Proceedings of the Seventh International Conference on
Railway Technology: Research, Development and Maintenance
Edited by: J. Pombo
Civil-Comp Conferences, Volume 15, Paper 19.5
Civil-Comp Press, Edinburgh, United Kingdom, 2026
ISSN: 2753-3239, doi: 10.4203/ccc.15.19.5

A 2.5D Coupled BEM Approach for the Analysis of Low-Height Railway Noise Barriers

R. Velazquez-Mata[1], P. Galvín[1], A. Romero[1] and A. Tadeu[2]

[1] Escuela Técnica Superior de Ingeniería, Universidad de Sevilla, Spain
[2] Departamento de Engenharia Civil, Universidade de Coimbra, Portugal

Abstract

This work presents a numerical study on the effectiveness of low-height barriers for railway noise mitigation. A 2.5D coupled solid-fluid formulation based on the Boundary Element Method is adopted to model the interaction between the track system and the surrounding acoustic field in an unbounded domain. The approach allows the simultaneous representation of the rail, the supporting pad, the fluid medium and additional acoustic boundaries, such as barriers and simplified vehicle envelopes.

The methodology is applied to a UIC60 rail supported on a rail pad and excited by a unit vertical point load. Several low-height barrier configurations are analysed, considering different geometrical layouts and the presence of the vehicle. The acoustic response is evaluated in terms of sound pressure level and insertion loss.

The analysed cases highlight the role of low-height barrier shape in the redistribution of the radiated field, as well as the contribution of the vehicle to the associated noise encapsulation effect. The proposed model provides a suitable

numerical tool for the comparative analysis of near-track railway noise mitigation solutions.

Keywords: railway noise mitigation, low-height barrier, boundary element method, 2.5D formulation, rolling noise, insertion loss

1 Introduction

Environmental noise has become a major concern, further intensified by the expansion of high-speed railway systems and their increasing presence in urban and peri-urban environments. In this context, accurate prediction of noise levels is essential for the design of effective mitigation measures. Noise barriers are widely used to reduce sound propagation from railway sources, although conventional solutions often require significant height and space, leading to increased land use and the creation of physical and visual discontinuities within the urban environment. Alternative solutions, such as low-height barriers placed close to the track, aim to reduce these effects while maintaining noise attenuation by confining sound radiation near the source and limiting both spatial requirements and visual impact.

Railway noise arises from different mechanical and aerodynamic sources, although in many practical situations the dominant contribution is rolling noise. This is generated by the wheel-rail interaction, which induces vibrations in the track and their subsequent radiation into the surrounding air domain. Consequently, the evaluation of barrier effectiveness involves the resolution of a vibro-acoustic problem in an unbounded environment.

In order to address this problem, numerical approaches based on the Boundary Element Method provide an efficient formulation, as they require discretization only of the boundaries. In this work, a 2.5D coupled solid–fluid formulation is adopted to model the interaction between the track and the acoustic field, enabling the simultaneous representation of the railway track, the surrounding air, and noise barriers within a single model. This formulation is used to analyse the effectiveness of noise barriers and to evaluate the influence of their geometrical configuration, with the aim of identifying optimal design solutions.

2 Numerical model

A coupled solid-fluid model (Ω) is considered to analyse sound radiation from railway systems and its interaction with noise barriers. As shown in Figure 1, the computational domain is divided into subdomains including the solid track components, such as the rail (Ω_{s_1}) and rail pad (Ω_{s_2}), and the fluid domain (Ω_f) representing the surrounding air. The approach is not restricted to these components, and additional solid subdomains can be incorporated when required for a more detailed representation of the track system. Likewise, extra boundaries such as noise barriers or railway vehicle boundaries can be introduced within the acoustic domain to evaluate their influence on sound radiation.

Each subdomain is modelled using the Boundary Element Method. Assuming invariance along the z-direction, the problem is solved in the frequency-wavenumber domain $(\omega - \kappa_z)$ employing a two-and-a-half-dimensional (2.5D) formulation [1]:

$$\mathbf{a}(\mathbf{x},\omega) = \int_{-\infty}^{+\infty} \widetilde{\mathbf{a}}(\widetilde{\mathbf{x}},\kappa_z,\omega) e^{-\iota\kappa_z z}\, d\kappa_z \tag{1}$$

where $\widetilde{\mathbf{a}}(\widetilde{\mathbf{x}},\kappa_z,\omega)$ is the frequency-wavenumber representation of a variable of interest such as displacement or sound pressure, ω is the angular frequency, $\mathbf{x} = (x, y, z)$ and $\widetilde{\mathbf{x}} = \mathbf{x}(x, y, 0)$. The Greek letter ι denotes the unit imaginary number.

The solution of the coupled air-track system is obtained by imposing appropriate conditions at the solid-solid and solid-fluid interfaces. Equilibrium of forces and compatibility of displacements must be achieved at solid interfaces; and the equilibrium of normal pressure, with null shear stress, and continuity of normal displacement are imposed at the solid-fluid interface Γ_{sf}. Each subdomain is directly coupled, and the equations are assembled into a global system.

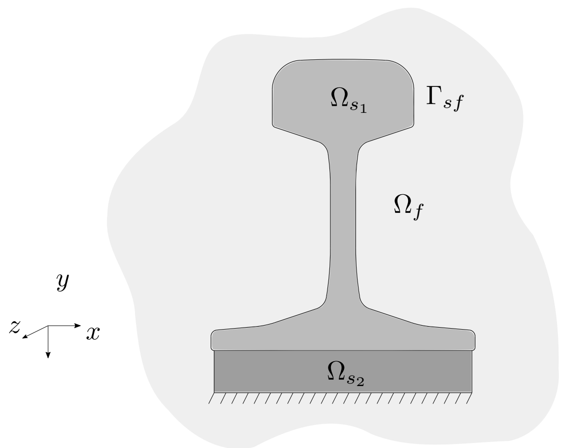

Figure 1: Boundary subdomains definition: rail (Ω_{s_1}), rail pad (Ω_{s_2}) and air medium (Ω_f).

2.1 Boundary element formulation in elastodynamics

The solid components of the railway system are modelled using the BEM formulation in elastodynamics. Assuming the absence of body forces, the boundary integral equation for the displacement field at a collocation point $\widetilde{\mathbf{x}}_i$ can be written as follows [2]:

$$
\begin{aligned}
\mathbf{c}_i(\widetilde{\mathbf{x}}_i)\widetilde{\mathbf{u}}_i(\widetilde{\mathbf{x}}_i,\kappa_z,\omega) = \int_{\Gamma_s} \Big(&\widetilde{\mathbf{t}}(\widetilde{\mathbf{x}},\kappa_z,\omega)\widetilde{\mathcal{G}}(\widetilde{\mathbf{x}},\kappa_z,\omega;\widetilde{\mathbf{x}}_i) \\
&- \widetilde{\mathbf{u}}(\widetilde{\mathbf{x}},\kappa_z,\omega)\widetilde{\mathcal{H}}(\widetilde{\mathbf{x}},\kappa_z,\omega;\widetilde{\mathbf{x}}_i)\Big)\, d\Gamma(\widetilde{\mathbf{x}})
\end{aligned}
\tag{2}
$$

where $\widetilde{\mathbf{u}}(\widetilde{\mathbf{x}},\kappa_z,\omega)$ and $\widetilde{\mathbf{t}}(\widetilde{\mathbf{x}},\kappa_z,\omega)$ are displacement and traction, respectively. $\widetilde{\mathcal{G}}(\widetilde{\mathbf{x}},\kappa_z,\omega;\widetilde{\mathbf{x}}_i)$ and $\widetilde{\mathcal{H}}(\widetilde{\mathbf{x}},\kappa_z,\omega;\widetilde{\mathbf{x}}_i)$ are the full-space fundamental solution to displacement and traction at the point $\widetilde{\mathbf{x}}$ due to a point source acting at the collocation point $\widetilde{\mathbf{x}}_i$. The integral-free term $\mathbf{c}_i(\widetilde{\mathbf{x}}_i)$ depends only on the boundary geometry at the collocation point $\widetilde{\mathbf{x}}_i$.

The two-and-a-half-dimensional Green's function is obtained by means of the potentials $\tilde{A}_p$ and $\tilde{A}_s$ for the irrotational and equivoluminal parts of the displacement vector, respectively [3]:

$$
\tilde{A}_p = \frac{\iota}{4\rho\omega^2}\left[H_0^{(2)}(\kappa_\alpha r) - H_0^{(2)}(-\iota\kappa_z r)\right] \tag{3}
$$

$$
\tilde{A}_s = \frac{\iota}{4\rho\omega^2}\left[H_0^{(2)}(\kappa_\beta r) - H_0^{(2)}(-\iota\kappa_z r)\right] \tag{4}
$$

where $\kappa_\alpha = \sqrt{\kappa_p^2 - \kappa_z^2}$ and $\kappa_\beta = \sqrt{\kappa_s^2 - \kappa_z^2}$, and κ_p and κ_s represent the wavenumbers for dilatational and shear waves, respectively. $H_0^{(2)}$ is the Hankel function of the second kind. Thus, the displacement $\widetilde{\mathcal{G}}_{kl}(\widetilde{\mathbf{x}},\kappa_z,\omega;\widetilde{\mathbf{x}}_i)$ in the k direction at $\widetilde{\mathbf{x}}$ due to a point load with acting in the l direction at $\widetilde{\mathbf{x}}_i$ is obtained from:

$$
\widetilde{\mathcal{G}}_{kl}(\widetilde{\mathbf{x}},\kappa_z,\omega;\widetilde{\mathbf{x}}_i) = \frac{\partial^2(\tilde{A}_p - \tilde{A}_s)}{\partial x_k \partial x_l} + \delta_{kl}\tilde{\nabla}^2\tilde{A}_s \tag{5}
$$

2.2 Boundary element formulation in fluid-acoustics

The surrounding air is represented by the fluid domain, where additional boundaries such as noise barriers and the railway vehicle envelope can be incorporated. The integral representation of the sound pressure in the frequency-wavenumber domain for a point $\widetilde{\mathbf{x}}_i$ located at the boundary Γ_{sf} can be written as [1]:

$$
\begin{aligned}
c_i(\widetilde{\mathbf{x}}_i)\widetilde{p}_i(\widetilde{\mathbf{x}}_i,\kappa_z,\omega) = -\int_{\Gamma_{sf}} \Bigg(&\iota\rho\omega\widetilde{v}(\widetilde{\mathbf{x}},\kappa_z,\omega)\widetilde{\Psi}(\widetilde{\mathbf{x}},\kappa_z,\omega;\widetilde{\mathbf{x}}_i) \\
&+ \widetilde{p}(\widetilde{\mathbf{x}},\kappa_z,\omega)\frac{\partial\widetilde{\Psi}(\widetilde{\mathbf{x}},\kappa_z,\omega;\widetilde{\mathbf{x}}_i)}{\partial\mathbf{n}}\Bigg)\, d\Gamma(\widetilde{\mathbf{x}})
\end{aligned}
\tag{6}
$$

where $\widetilde{p}(\widetilde{\mathbf{x}},\kappa_z,\omega)$ and $\widetilde{v}(\widetilde{\mathbf{x}},\kappa_z,\omega)$ are the sound pressure and the particle normal velocity at the boundary Γ_{sf}, respectively. $\widetilde{\Psi}(\widetilde{\mathbf{x}},\kappa_z,\omega;\widetilde{\mathbf{x}}_i)$ represents the velocity potential at point $\widetilde{\mathbf{x}}$ due to a point source located at $\widetilde{\mathbf{x}}_i$:

$$\widetilde{\Psi}(\widetilde{\mathbf{x}}, \kappa_z, \omega; \widetilde{\mathbf{x}}_i) = -\frac{\iota}{4} H_0^{(2)}(\kappa_f r) \tag{7}$$

where $\kappa_f = \sqrt{(\omega/c_f)^2 - \kappa_z^2}$ is the fluid wavenumber, c_f is the sound propagation velocity, and $H_0^{(2)}$ is the Hankel function of the second kind.

2.3 Geometry and element approximation

An accurate definition of the geometry is essential for the description of complex track systems and for the evaluation of their contribution to noise radiation. It is also particularly relevant when analysing noise barriers, since their acoustic effect is strongly influenced by their shape and position.

In this work, the BEM formulations are implemented in the Bézier-Bernstein space [1], where the Bézier-Bernstein polynomial form is used as a common basis to represent both the exact CAD-based geometry and the independently approximated field variables. The Bézier curve $\mathbf{r}_n(t)$ is expressed as:

$$\mathbf{r}_n(t) = \sum_{k=0}^{n} \mathbf{b}_k B_k^n(t) \tag{8}$$

where $\mathbf{b}_k$ are the control points used to approximate the geometry and n is the curve degree. An efficient curve computation is achieved using the polar form of a Bézier curve $\mathbf{r}_n(t)$, which defines a multiaffine transformation satisfying:

$$\mathbf{b}_k = \mathbf{R}(\underbrace{0, \ldots, 0}_{n-k}, \underbrace{1, \ldots, 1}_{k}) \tag{9}$$

where $\mathbf{R}(t_1, \ldots, t_n)$ is computed as:

$$\mathbf{R}(t_1, \ldots, t_n) = \sum_{\substack{I \cap J = \emptyset \\ I \cup J = \{1,2,\ldots,n\}}} \prod_{i \in I} (1 - t_i) \prod_{j \in J} t_j \mathbf{b}_{|J|} \tag{10}$$

Thus, a Bernstein polynomial can be formulated in polar form substituting Equation (9) into Equation (8) as follows:

$$\mathbf{r}_n(t) = \sum_{k=0}^{n} \mathbf{R}(\underbrace{0, \ldots, 0}_{n-k}, \underbrace{1, \ldots, 1}_{k}) B_k^n(t) = \mathbf{R}(t, \ldots, t) \tag{11}$$

The Bézier-Bernstein space is used to describe the exact element geometry as $\Gamma^j(\mathbf{x}) = \mathbf{r}_n^j(t)$. Hence, the element integrals can be written on an univariate basis $t \in [0, 1]$ as [1]:

$$\int_{\Gamma^j} f(\widetilde{\mathbf{x}}, \kappa_z, \omega; \widetilde{\mathbf{x}}_i)\, d\Gamma = \int_0^1 f(\widetilde{\mathbf{x}}(t), \kappa_z, \omega; \widetilde{\mathbf{x}}_i) \left| \frac{d\mathbf{r}_n^j(t)}{dt} \right| dt \tag{12}$$

where $f(\widetilde{\mathbf{x}}, \kappa_z, \omega; \widetilde{\mathbf{x}}_i)$ represents the integration kernel.

The BEM formulation in the Bézier-Bernstein space employs the Lagrange interpolant relative to the Bernstein basis for the field variable approximation to an element. The field approximation given by the shape function interpolates $(n+1)$ nodal values through the element shape functions ϕ^i of order n, for $i = 0, \ldots, n$. Then, the field approximation becomes:

$$a(t) = \sum_{i=0}^{p} \phi^i(t) a^i = \sum_{i=0}^{p} \left\{ \sum_{k=0}^{n} c_k^i B_k^n(t) \right\} a^i = \sum_{i=0}^{p} R^i(t, \ldots, t) a^i, \tag{13}$$

where the evaluation of the element shape function $\phi^i(t)$ also benefits from the computational advantages of using the polar form $R^i(t_1, \ldots, t_n)$ according to Equation (10).

After introducing the geometry and field approximations from Equations (11) and (13) into each subdomain's boundary integral equation, integrals are computed using standard Gauss-Legendre quadrature with $(p+1)$ points when the collocation point is sufficiently far from the element. For singular or weakly singular integrals, numerical evaluation is performed using the quadrature method described in [1, 4].

Then, Equations (2) and (6) are rewritten as follows:

$$\widetilde{\mathbf{H}}_s(\widetilde{\mathbf{x}}, \kappa_z, \omega; \widetilde{\mathbf{x}}_i) \widetilde{\mathbf{u}}(\widetilde{\mathbf{x}}, \kappa_z, \omega) = \widetilde{\mathbf{G}}_s(\widetilde{\mathbf{x}}, \kappa_z, \omega; \widetilde{\mathbf{x}}_i) \widetilde{\mathbf{t}}(\widetilde{\mathbf{x}}, \kappa_z, \omega) \tag{14}$$

$$\widetilde{\mathbf{H}}_f(\widetilde{\mathbf{x}}, \kappa_z, \omega; \widetilde{\mathbf{x}}_i) \widetilde{p}(\widetilde{\mathbf{x}}, \kappa_z, \omega) = \widetilde{\mathbf{G}}_f(\widetilde{\mathbf{x}}, \kappa_z, \omega; \widetilde{\mathbf{x}}_i) \widetilde{v}(\widetilde{\mathbf{x}}, \kappa_z, \omega) \tag{15}$$

where $\widetilde{\mathbf{H}}_s$, $\widetilde{\mathbf{G}}_s$, $\widetilde{\mathbf{H}}_f$ and $\widetilde{\mathbf{G}}_f$ are the fully non-symmetrical boundary element system matrices for solids and acoustic subdomains, respectively.

2.4 Subdomains coupling procedure

Solid subdomains such as rail and rail pads are coupled imposing equilibrium of forces and compatibility of displacements at solid interfaces. Equilibrium of forces at the interface is fulfilled integrating nodal tractions according to the element shape function $\mathbf{N} = [\phi_0, \ldots, \phi_p]$:

$$\widetilde{\mathbf{f}} = \int_{\Gamma_s} \mathbf{N}^T \widetilde{\mathbf{t}} \mathbf{N} \, d\Gamma = \mathbf{T} \widetilde{\mathbf{t}} \tag{16}$$

Substituting Equation (16) into Equation (14) yields the following.

$$\widetilde{\mathbf{f}} = \mathbf{T} \widetilde{\mathbf{G}}_s^{-1} \widetilde{\mathbf{H}}_s \widetilde{\mathbf{u}} \tag{17}$$

Then the coupled system for solid subdomains is obtained imposing the equilibrium and compatibility conditions at the interface:

$$\widetilde{\mathbf{K}}_s(\widetilde{\mathbf{x}}, \kappa_z, \omega; \widetilde{\mathbf{x}}_i) \widetilde{\mathbf{u}}(\widetilde{\mathbf{x}}, \kappa_z, \omega) = \widetilde{\mathbf{f}}(\widetilde{\mathbf{x}}, \kappa_z, \omega) \tag{18}$$

The solid and fluid subdomains are assembled by coupling Equations (15) and (18) through the enforcement of equilibrium and compatibility conditions of normal pressure and displacement at the interface Γ_{sf} between the track system and the air medium, and null shear stresses. This coupling yields the following system of equations [5]:

$$\begin{bmatrix} \widetilde{\mathbf{K}}_s & \mathbf{R}^T \\ -\widetilde{\mathbf{G}}_f\mathbf{N}^T & \widetilde{\mathbf{H}}_f \end{bmatrix} \begin{bmatrix} \widetilde{\mathbf{u}} \\ \widetilde{p} \end{bmatrix} = \begin{bmatrix} \widetilde{\mathbf{f}} \\ 0 \end{bmatrix} \tag{19}$$

where $\mathbf{R}$ is the coupling fluid–solid matrix which relates force and pressure at the interface Γ_{sf}:

$$\widetilde{\mathbf{f}} = -\int_{\Gamma_{sf}} \mathbf{N}^T \mathbf{n} c \widetilde{p}\, d\Gamma = \mathbf{R}^T \widetilde{p} \tag{20}$$

where $\mathbf{n}$ is the outward normal vector at Γ_{sf}.

3 Numerical example

In this section, the proposed methodology is applied to analyse the effectiveness of low-height barriers for railway noise mitigation. The reference track configuration consists of a UIC60 rail supported on a 10 cm thick rail pad, as shown in Figure 2. The material properties of the track components are listed in Table 1. The system is excited by a unit vertical point load applied at the centre of the railhead. In order to simplify the analysis and avoid the additional interference associated with a two-rail configuration, only a single rail is considered.

Four barrier configurations are analysed, all of them located at 1.70 m from the track axis, which corresponds to 0.98 m from the centre of the analysed rail. The first configuration consists of a curved low-height barrier with a total height of 1.60 m. The second configuration corresponds to the same curved barrier combined with a simplified Renfe S-103 vehicle envelope. The third configuration considers a low-height barrier with the same base geometry, but with the upper part replaced by a single straight segment inclined at 40° from the vertical, while the fourth one consists of a straight low-height barrier with the same total height. The configurations including the vehicle are especially relevant, since one of the main features of low-height barriers is their ability to take advantage of the noise encapsulation effect produced by the presence of the vehicle. In all cases, the barrier and vehicle boundaries are treated as reflecting surfaces, imposing zero normal velocity conditions.

The acoustic response is evaluated in terms of sound pressure level and insertion loss, comparing each mitigation configuration with the reference case without barrier. Particular attention is given to the influence of barrier geometry and vehicle presence on the radiated acoustic field.

Figure 3 shows the insertion loss obtained at 1400 Hz for the analysed barrier configurations. The results highlight the influence of the vehicle on the acoustic

	Rail	**Rail pad**
Young's modulus [MPa]	210×10^3	3.2
Density [kg/m^3]	7860	1000
Poisson's ratio [-]	0.3	0.45
Damping loss factor [-]	0.02	0.25

Table 1: Material properties for the track system.

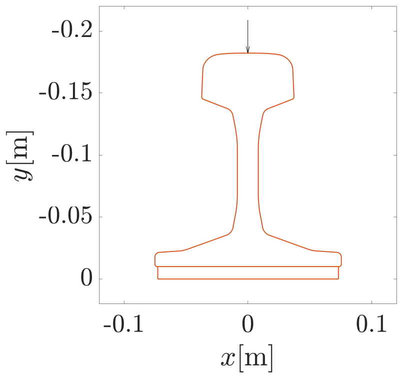

Figure 2: Model geometry and load application point for the track system.

field, since its presence promotes a partial encapsulation effect. However, as both the barrier and the vehicle have been modelled as fully reflective boundaries, the wave field is redistributed and, in some cases, the attenuation behind the barrier is reduced due to additional reflections. The results reveal clear similarities between the curved barrier and the two-segment configuration, which suggests that both geometries lead to a comparable redirection of the radiated field. By contrast, the straight barrier exhibits lower insertion loss levels, mainly due to the gap between the vehicle and the barrier, which facilitates wave propagation towards the region behind the barrier.

The sound pressure levels and insertion loss obtained at a receiver located 2 m from the rail axis and 1.20 m above the railhead are shown in Figure 4. A reduction in sound pressure level is observed in all mitigation cases, although its magnitude depends strongly on frequency. At low frequencies, the configurations including the vehicle generally provide greater insertion loss, since the gap between the barrier and the vehicle is less effective in transmitting long wavelengths and the encapsulation effect becomes more noticeable. A similar behaviour is observed for the curved and two-segment barriers at low frequencies, due to the similarity of their upper geometry. At higher frequencies, the differences between both configurations become more pronounced, highlighting the importance of barrier shape in the scattering and redistribution of the acoustic field. The straight barrier shows the lowest insertion loss at low frequencies and, at higher frequencies, exhibits similar reflective behaviour as the other cases.

The results confirm the strong influence of barrier geometry and vehicle pres-

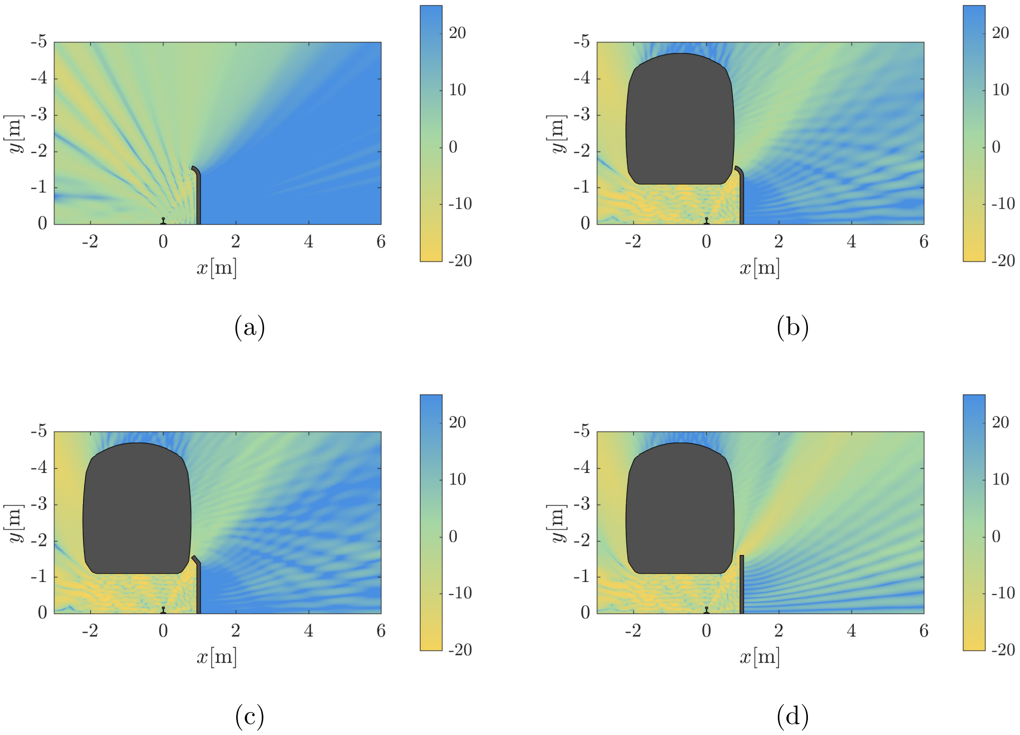

Figure 3: Insertion loss (dB) at 1400 Hz: (a) with a low-height curved barrier, and including Renfe S-103 vehicle: (b) with a low-height curved barrier, (c) with a low-height two-segment inclined barrier and (d) with a low-height straight barrier.

ence on the acoustic performance of low-height barriers. The proposed model provides a suitable tool for the comparative analysis of these mitigation concepts. A more complete assessment would require extending the study to include absorptive boundary conditions, different material properties and additional distances from the rail axis.

4 Conclusions

This work has presented a 2.5D coupled solid-fluid formulation based on the Boundary Element Method for the analysis of railway noise barriers. The proposed approach allows the track system, the surrounding acoustic field and additional boundaries, such as noise barriers and railway vehicle envelopes, to be represented within the same numerical model.

The methodology has been applied to the study of several low-height barrier configurations, with particular attention to the influence of barrier geometry and vehicle presence on the radiated acoustic field. The results show that both factors have a significant effect on the spatial distribution of sound pressure and on the

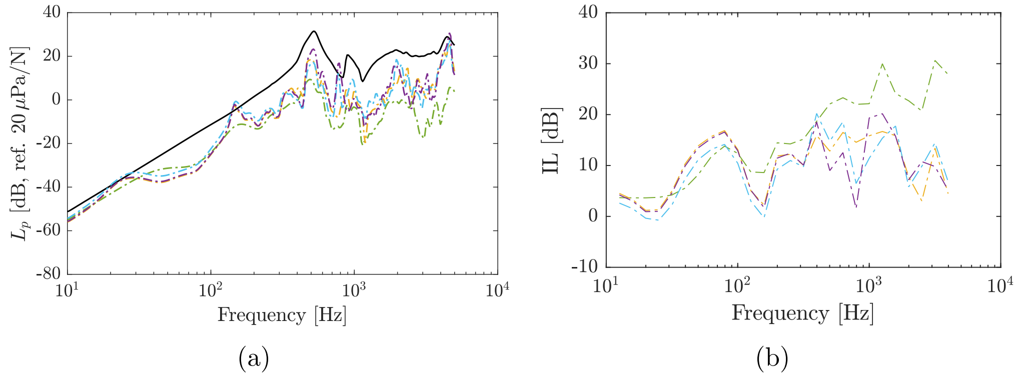

Figure 4: (a) Sound pressure levels (L_p) and (b) acoustic insertion loss (IL) at 1.20 m above the railhead under different conditions: (solid black) no barrier and (dash-dotted) low-height barriers: (green) curved, and including Renfe S-103 vehicle: (yellow) curved, (purple) two-segment inclined, and (blue) straight. Results correspond to $x = 2\,\mathrm{m}$.

resulting insertion loss.

The analysed cases indicate that low-height barriers can provide an effective mitigation mechanism, especially when combined with the vehicle, due to the associated noise encapsulation effect. At the same time, the results highlight that this effect strongly depends on the barrier geometry, since different upper shapes lead to different reflection and scattering patterns. In this regard, the curved and two-segment configurations show a similar behaviour in part of the analysed frequency range, whereas the straight barrier generally provides lower insertion loss.

These results confirm that the geometrical design of low-height barriers plays a key role in their acoustic effectiveness. The proposed formulation therefore provides a suitable tool for the comparative assessment and design of near-track mitigation solutions. Further work should include absorptive boundary conditions, more realistic material properties and an extended parametric analysis including other receiver positions and barrier layouts.

Acknowledgements

The authors acknowledge the following institutions for their financial support: Spanish Ministry of Science and Innovation, Agencia Española de la Investigación (AEI), and FEDER EU Funds (PID2022-138674OB-C2). The authors also acknowledge the Institute of Sound and Vibration Research (ISVR) for hosting the research stay that contributed to this work.

References

[1] Romero A, Galvín P, Cámara-Molina JC, Tadeu A. On the formulation of a BEM in the Bézier–Bernstein space for the solution of Helmholtz equation. Applied Mathematical Modelling. 2019;74:301-19. Available from: https://www.sciencedirect.com/science/article/pii/S0307904X19302720.

[2] Romero A, Tadeu A, Galvín P, António J. 2.5D coupled BEM–FEM used to model fluid and solid scattering wave. International Journal for Numerical Methods in Engineering. 2015;101(2):148-64. Available from: https://onlinelibrary.wiley.com/doi/abs/10.1002/nme.4801.

[3] Tadeu AJB, Kausel E. Green's Functions for Two-and-a-Half-Dimensional Elastodynamic Problems. Journal of Engineering Mechanics. 2000;126(10):1093-7.

[4] Velázquez-Mata R, Romero A, Domínguez J, Tadeu A, Galvín P. A novel high-performance quadrature rule for BEM formulations. Engineering Analysis with Boundary Elements. 2022;140:607-17. Available from: https://www.sciencedirect.com/science/article/pii/S095579972200145X.

[5] Cruz-Muñoz FJ, Romero A, Galvín P, Tadeu A. Acoustic waves scattered by elastic waveguides using a spectral approach with a 2.5D coupled boundary-finite element method. Engineering Analysis with Boundary Elements. 2019;106:47-58. Available from: https://www.sciencedirect.com/science/article/pii/S0955799718307732.